Magnetic Resonance in Medicine 65:1062–1075 (2011)

''PINOT'': Time-Resolved Parallel Magnetic Resonance Imaging With a Reduced Dynamic Field of View

Lei Hou Hamilton,[1] Javier Acebron Fabregat,[2] David Moratal,[2] Senthil Ramamurthy,[3] Stamatios Lerakis,[3] W. James Parks,[3,4] Denver Sallee, III,[3,4] and Marijn E. Brummer[3]*

This article introduces a novel method named "Parallel Imaging and NOquist in Tandem" (PINOT) for accelerated image acquisition of cine cardiac magnetic resonance imaging. This method combines two prior information formalisms, the SPACE-RIP implementation of parallel imaging and the Noquist method for reduced-data image reconstruction with prior knowledge of static and dynamic regions in the field of view. The general theory is presented, and supported by results from experiments using time-resolved two-dimensional simulation data and retrospectively sub-sampled magnetic resonance imaging data with acceleration factors around 4. A signal-to-noise ratio analysis and a comparison study with TSENSE and *k-t* SENSE show that PINOT performs favorably in preserving edge detail, at a cost in signal-to-noise ratio and computational complexity. Magn Reson Med 65:1062–1075, 2011. © 2010 Wiley-Liss, Inc.

Key words: magnetic resonance imaging; dynamic imaging; image reconstruction; Noquist; parallel imaging

Imaging speed is important in dynamic cardiac applications to overcome motion artifacts. Patient safety considerations limit further use of faster gradients or higher radiofrequency power to speed up the pulse sequence beyond current technology. Various methods have been proposed to increase the imaging speed by reducing the sampling rate through incorporation of prior information in the image reconstruction. Parallel imaging methods exploit redundancy in spatial encoding in image acquisitions with signals from multichannel receiver systems, where each receiver channel has known and at least partially independent spatial sensitivity characteristics. SMASH (1), AUTO-SMASH (2), VD-AUTO-SMASH (3), and GRAPPA (4) synthesize missing *k*-space samples from acquired samples at other locations to construct a complete grid. PILS (5), SENSE (6), and SPACE-RIP (7) use estimates of the coil sensitivity maps to reconstruct the image from reduced *k*-space samples. The maximum sampling rate reduction factor is limited by the number of independent channels (8,9). However, this maximum is usually not achieved due to noise amplification or imperfections in the sensitivity maps. Recent improvements have focused on improving accuracy of sensitivity maps. Ying and Sheng (10) and Uecker et al. (11) both apply joint iterative estimation of the image and the sensitivity maps. GEYSER (12) uses GRAPPA to improve coil calibration for SENSE-like techniques.

Spatiotemporal redundancy in dynamic imaging may be exploited if parts of the field of view (FOV) are relatively static over time. UNFOLD (13) employs time interleaving of *k*-space lines to remove data redundancy from time-varying objects using a temporal filter. Noquist (14) exploits the data redundancy associated with the presence of a static FOV region by only reconstructing it once for a dynamic sequence. It uses a direct inversion model without temporal filtering or interpolation. The reduction factor for these methods is limited by the ratio of the size of the static region to the total FOV. *k-t* BLAST samples the *k-t* space (spatial frequency and time) sparsely on a lattice grid, signal aliasing will be shifted in the reciprocal *x-f* space. A low-resolution estimate of the signal distribution in *x-f* space is obtained using training data, and used to separate the true signal from the aliased copies in the undersampled data.

These two separate prior information sources may be combined for even higher gains in imaging speed. TSENSE, as initially proposed (15), uses UNFOLD to eliminate residual aliasing artifacts that were not removed by SENSE. Subsequent improvements (16) combine UNFOLD and SENSE for compounded gains from each method. UNFOLD-SENSE (17) combines variable-density SENSE with self-calibration for sensitivity map estimation. TGRAPPA (18) uses time-interleaved sampling with improved acquisition efficiency. *k-t* SENSE (19) allows high-reduction factors by combining *k-t* BLAST with SENSE parallel imaging.

All fast imaging methods discussed above carry a price for the higher imaging speed, in comparison with conventional fully sampled imaging. This may be a signal-to-noise ratio (SNR) penalty, reduced spatio-temporal resolution, or a combination of these two. Depending on the ''native'' SNR and resolution of the comparable fully sampled conventional scan, a method with desired characteristics may be selected. Methods with SNR penalties may sometimes be improved by regularization techniques to shift their characteristics toward better problem conditioning, trading off resolution. The converse does not hold in all cases: methods which intrinsically rely on filtering or regularization may not always be ''unregularized'' to

[1]School of Electrical and Computer Engineering, Georgia Institute of Technology, Atlanta, Georgia, USA.

[2]Center for Biomaterials and Tissue Engineering, Universitat Politècnica de València, Valencia, Spain.

[3]School of Medicine, Emory University, Atlanta, Georgia, USA.

[4]Sibley Heart Center Cardiology, Atlanta, Georgia, USA.

Grant sponsor: National Institute of Health (NIH); Grant number: R01 HL077627.

*Correspondence to: Marijn E. Brummer, PhD, Departments of Pediatrics/Children's Research Center, Emory University School of Medicine, 2015 Uppergate Drive, Atlanta, Georgia 30322. E-mail: mbrumme@emory.edu

Received 23 October 2009; revised 6 August 2010; accepted 28 September 2010.

DOI 10.1002/mrm.22696

Published online 30 November 2010 in Wiley Online Library (wileyonlinelibrary.com).

regain better resolution. If image resolution is the most critical criterion, reduced-data methods which allow full or nearly full preservation of ''full-grid resolution'' may present the preferred approach. SENSE, SPACE-RIP, and Noquist all possess such characteristics. Interestingly, none of the proposed combined techniques are capable of reconstructing the image at the same spatiotemporal resolution as the fully sampled grid due to the use of filter or interpolation, even if the reduced data sets still represent an overdetermined inversion problem.

In this article, we present a method ''Parallel Imaging and NOquist in Tandem'' (PINOT), introduced earlier under the provisional name ''No'nSENSE'' (20), which combines the SPACE-RIP parallel imaging method and the Noquist (rFOV method). SPACE-RIP and Noquist use similar approaches in *k*-space, and combine naturally into an integrated approach. As a corollary, it preserves advantages and challenges of both methods. If the underlying model conditions are satisfied PINOT fully preserves spatial and temporal resolution of the full-grid acquisition. In exchange, it carries a higher penalty in SNR and increased computational cost. SNR characteristics can be moderated by regularization, but this is not an intrinsic feature of the method and may be omitted given sufficiently well-posed problem conditions and low-noise data. In the next section, we introduce theoretical aspects of PINOT, followed by experimental results on computer simulated data and retrospectively sub-sampled full-grid magnetic resonance imaging (MRI) data. These results are put in further perspective by a comparison of PINOT with the individual SPACE-RIP and Noquist methods, and by a comparison with TSENSE and *k-t* SENSE.

MATERIALS AND METHODS

The PINOT Imaging Method

During acquisition of a cine image, *k*-space sampling points *F(k,t)* are acquired at multiple time points *t* in the cardiac cycle. In conventional serial imaging with rectilinear *k*-space sampling, trains of the same read-out sampling points are acquired at each phase encoding value to cover a *k*-space grid in identical fashion at each time point. Fourier inversion reconstructs the images *f(x,t)*. Reduced sampling in the read-out dimension does not offer much imaging time savings, but imaging time is linearly proportional to the number of phase encodings. Therefore, fast imaging methods often focus on reducing the number of phase encodings. Read-out reconstruction is performed conventionally by discrete Fourier transfrom (DFT), whereas appropriate algorithms must be developed for modified phase encoding reconstruction from reduced samples. Thus, the 2D spatial image reconstruction problem may be reduced to a 1D spatial problem, only considering the phase encoding and time dimensions.

Parallel Imaging

Parallel imaging methods reconstruct the image f from reduced-sampled data acquired from multiple coils, assuming each coil provides independent additional spatial image information. Considering temporal and coil information together for a dynamic image sequence *f(x,t)*, the MR signal F_c received for cardiac delay time t in coil c, with S_c sensitivity map, is:

$$F_c(k,t) = \sum_{x=0}^{N-1} S_c(x) f(x,t) \varphi(x,k) \quad [1]$$

N is the number of phase encoding views, k and φ $(x,k) = e^{-j2\pi kx}$ are the Fourier coefficients. Expressed in matrix form:

$$F = Mf \quad [2]$$

where vector F contains the k-space data of all N_c coils and phase encodings for time frame t, and M is the forward system matrix. Conventional image reconstruction does not invert the coil modulation S_c, and reconstructs the modulated function $f_S = S_c f$ by Fourier inversion:

$$f_S = \Omega^{-1} F \quad [3]$$

where Ω^{-1} contains the inverse Fourier coefficients.

In parallel imaging, M contains both the coil sensitivity information S and the Fourier coefficients:

$$M_p = S\Omega \quad [4]$$

If the sensitivity maps S are known, Eq. 4 is an overdetermined linear system. It may be sampled below Nyquist rate provided M_p has a pseudoinverse. Let us define a data reduction factor R relative to full-grid Fourier encoding, i.e., for parallel imaging $R_p = N/N_{sample\_p}$ where N_{sample_p} is the number of sampled phase encodings, or parallel imaging. M is of size $N_c\ N_{sample\_p} \times N$, hence for M_p to remain invertible the reduction factor R_p must be

$$R_p \leq N_c \quad [5]$$

Of particular interest in this work, due to compatibility with the Noquist model [see (14), and next paragraph], the SPACE-RIP parallel imaging method (7) finds the solution by pseudo-inversion of Eq. 2:

$$f = (M_p^H M_p)^{-1} M_p^H F \quad [6]$$

Noquist Imaging

If part of the FOV does not change over time, we can define the sizes of the static and dynamic portions of the FOV as N_S and N_D: $N = N_S + N_D$. If these sizes are known at acquisition (e.g., estimated from manual or automated observations in scout images), this allows us to reconstruct the static region only once for the entire sequence. The image vector f at a single time frame t can be partitioned as $f = [f_S^T\ f_{t,D}^T]^T$. Superscript T denotes transposition. The corresponding Fourier matrix can be similarly partitioned as $M = [M_S\ M_D]$. Data F_t for all T time frames indexed by t ($t \in \{0,1, \ldots, T-1\}$) may be concatenated into a single vector F:

$$F = \begin{bmatrix} F_0 \\ F_1 \\ \vdots \\ F_{T-1} \end{bmatrix} = \begin{bmatrix} M_S & M_D & \cdots & \cdots & 0 \\ M_S & 0 & M_D & \cdots & 0 \\ \vdots & \vdots & \vdots & \vdots & \vdots \\ M_S & 0 & 0 & \cdots & M_D \end{bmatrix} \begin{bmatrix} f_S \\ f_{0,D} \\ f_{1,D} \\ \vdots \\ f_{T-1,D} \end{bmatrix} = M_{Noquist} f. \quad [7]$$

The image sequence f is expressed as a vector, which concatenates the static portion of image followed by the dynamic portion for each time frame. $N_{\text{sample\_nq}}$ is defined as the reduced number of phase encoding samples, which should be equal for each time frame to ensure equidistant temporal sampling, so $N_{\text{data}} = N_{\text{sample\_nq}}\ T$. Because the static part f_S is only reconstructed once in Noquist, the total dynamic image size is $N_{\text{pixels}} = N_{\text{S}} + N_{\text{D}}\ T$. If the system matrix M_{noquist} with total size $N_{\text{data}} \times N_{\text{pixels}}$ is square, the image is reconstructed by multiplying the data F with its inverse:

$$f = M_{\text{Noquist}}^{-1} F \quad [8]$$

More generally, for over- or under-determined systems, the matrix inversion M^{-1} may be replaced by a Moore-Penrose pseudo-inverse (20). Exact solutions may exist for fully determined or overdetermined systems ($N_{\text{data}} \geq N_{\text{pixels}}$). It follows that

$$N_{\text{sample\_nq}} \geq N_{\text{S}}/T + N_{\text{D}} \quad [9]$$

Thus, the corresponding acceleration rate $R_{\text{nq}} = N/N_{\text{samples\_nq}}$ is maximized at

$$R_{\text{nq}} = N/(N_{\text{S}}/T + N_{\text{D}}) \quad [10]$$

The PINOT Method

The SPACE-RIP image reconstruction is a direct inversion of the weighted Fourier transform matrix, combined for all coils. Noquist also uses a direct inversion model. To implement accelerated imaging using both sources of prior knowledge, these two model formulations can be combined naturally into the PINOT method:

$$F = M_{\text{PINOT}} f \quad [11]$$

To alleviate the high-computational cost of using direct matrix inversion, iterative reconstruction algorithms, such as conjugate gradient method (21) may be used instead. The reconstructed image (column) vector f, with again the static region f_{S} only represented once, expands as

$$f = [f_{\text{S}}\ f_{0,\text{D}}\ f_{1,\text{D}}\ \cdots\ f_{T-1,\text{D}}]^T \quad [12]$$

The data vector F contains acquired phase encoded data k for all time frames and coils:

$$F = \left[F_{0,0}\ F_{0,1}\ \cdots F_{0,C-1}\ \cdots\ \cdots\ F_{T-1,0}\ F_{T-1,1}\ \cdots\ F_{T-1,C-1}\right]^T \quad [13]$$

k-space data F are now indexed by the time frame t as well as the coil c. The matrix M_{PINOT} is the forward system matrix for a given readout axis location. Its structure is similar to M_{Noquist}, but is expanded for all coils and weighted by sensitivity maps:

$$M_{\text{PINOT}} = \begin{bmatrix} M_{\text{S}}S_0 & M_{\text{D}}S_0 & 0 & \cdots & 0 \\ M_{\text{S}}S_1 & M_{\text{D}}S_1 & 0 & \cdots & 0 \\ \vdots & \vdots & \vdots & \vdots & \vdots \\ M_{\text{S}}S_{C-1} & M_{\text{D}}S_{C-1} & 0 & \cdots & 0 \\ M_{\text{S}}S_0 & 0 & M_{\text{S}}S_0 & \cdots & 0 \\ \vdots & \vdots & \vdots & \vdots & \vdots \\ M_{\text{S}}S_{C-1} & 0 & M_{\text{D}}S_{C-1} & \cdots & 0 \\ \vdots & \vdots & \vdots & \vdots & \vdots \\ M_{\text{S}}S_0 & 0 & 0 & \cdots & M_{\text{D}}S_0 \\ \vdots & \vdots & \vdots & \vdots & \vdots \\ M_{\text{S}}S_{C-1} & 0 & 0 & \cdots & M_{\text{D}}S_{C-1} \end{bmatrix} \quad [14]$$

The size of M_{PINOT} is $(TN_{\text{c}}N_{\text{sample\_PI}}) \times (TN_{\text{D}} + N_{\text{S}})$, where $N_{\text{sample\_PI}}$ denotes the number of phase encodings sampled for each time point. For a solvable system, the number of rows must again exceed the number of columns, thus

$$\left(TN_{\text{c}}N_{\text{sample\_PI}}\right) \geq (TN_{\text{D}} + N_{\text{S}}) \quad [15]$$

With R_{p} and R_{nq} defined as in Eqs. 5 and 10, this implies a minimum number of samples per time frame

$$N_{\text{sample\_PI}} = N/R_{\text{PINOT}} = N/R_{\text{p}}R_{\text{nq}} \geq (N_{\text{D}} + N_{\text{S}}/T)/N_{\text{C}} \quad [16]$$

for a solvable system. PINOT multiplicatively combines the maximum acceleration rates from parallel imaging and Noquist: $R_{\text{PINOT}} = R_{\text{p}}\ R_{\text{nq}}$. To maintain a solvable linear system of equations, the same data reduction limits apply as in the constituent methods.

Determination of Static and Dynamic FOV

Like Noquist, PINOT requires knowledge of the extent (at acquisition) and location (at reconstruction) of the static and dynamic FOV regions. In a practical implementation, these parameters can easily and quickly be derived from observation of moving structures in scout images, in conjunction with simple manual boundary delineation or possibly with automated detection of such boundaries. We note that, again similar to Noquist, any artifacts resulting from errors in the region boundaries may be corrected by repeating the reconstruction from the same undersampled data using corrected boundary locations, provided the dynamic region size is not underestimated.

PINOT Sampling in k-t Space

As discussed in (14,22) for Noquist, different sampling schemes can be designed for reduced sampling of *k-t* space. Not all patterns will yield a nonsingular and well-conditioned forward matrix M_{PINOT}. Similarly, reduced sampling for parallel imaging may be performed in different ways (6,7). Optimization of sampling schemes is a complex and important problem, which depends on a multitude of parameters such as coil sensitivity maps, spatiotemporal image characteristics, and other factors. PINOT further compounds this complexity by combining methods. We limit ourselves in this article to reporting

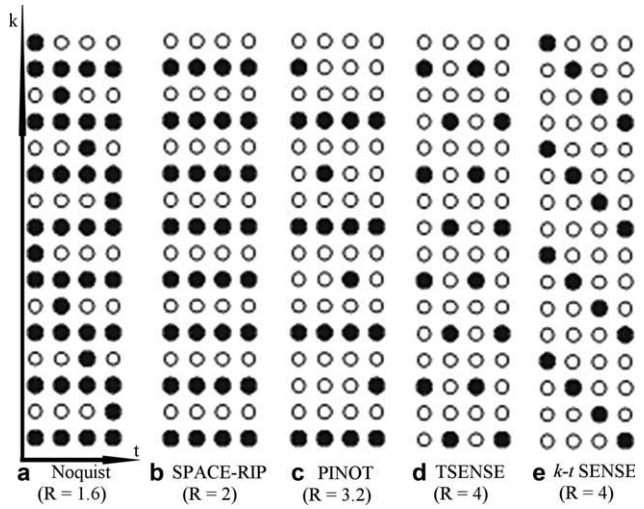

FIG. 1. Reduced sampling schemes for an example with 16 phase-encodings and four frames for (**a**) Noquist with 50% static FOV, (**b**) SENSE or SPACE-RIP, (**c**) PINOT, (**d**) TSENSE (not accounting for auto-calibrated lines), and (**e**) *k-t* BLAST/*k-t* SENSE (not accounting for training data). The horizontal axis represents time, and the vertical axis represents the phase encoding direction. The reduction factor *R* for each method is shown.

consistent success with a heuristically chosen sampling pattern. Optimization must be addressed appropriately in future research, but is considered outside the scope of this introductory paper. A stable subset selection method for Noquist with 50% dynamic FOV acquires even *k*-space lines in every frame and distributes acquisition of odd *k*-space lines across the phases of the cardiac cycle in a regular ''stairwell'' pattern (Fig. 1a). Similarly, a common subset sampling scheme for SENSE/SPACE-RIP with $R_p = 2$ is to simply acquire every other phase encoding view (6,7) (Fig. 1b). For PINOT, these sampling schemes are combined in a straightforward manner to form the pattern shown in Fig. 1c, which can readily be extended to larger grid sizes.

Experiments

We designed five experiments to demonstrate and evaluate PINOT's feasibility and performance. In the first experiment, PINOT was initially tested using noiseless computer simulated data. For reference, results for the same data with the individual SPACE-RIP and Noquist methods are also shown. To be more realistic, gaussian noise was added to the computer simulated data and sensitivity maps with uniform noise levels across all receiver channels and phase encoding views, at levels corresponding to 1% of highest root-sum-of squares image intensity, resulting in SNR in selected regions of interest (ROI) (shown in Fig. 3a) of 19.1482 dB, 17.6382 dB, and 15.4962 dB, respectively. PINOT ($R = 3.75$) was compared with corresponding SPACE-RIP and Noquist quantitatively (23,24) (see implementation details in Quantitative Performance Evaluation). Mean signal intensity and noise distribution images are shown. Normalized noise distributions of three methods are compared and shown in histogram, displayed separately for the static and dynamic region. To test the PINOT reconstruction robustness against different choices of static/dynamic FOV regions, PINOT reconstructions were performed at different acceleration factors, with varying static and dynamic regions ($R = 2.61$, 3.75, and 6.67). Noise distributions of different reduction factors are shown in histogram as well. Condition numbers, as a measure of how well-conditioned the M_{PINOT} is, are calculated with different reduction factors ($R = 3.75$, 6.67, and 13.33), reconstruction errors are defined as the Euclidean norm of difference between the reconstructed image and full-grid image.

In the second experiment, we tested PINOT on two real MRI data sets, in comparison with corresponding SPACE-RIP and Noquist for the first dataset in both spatial and temporal dimension. The second dataset showed PINOT reconstructions for different temporal frames.

The third experiment implemented TSENSE and *k-t* SENSE for comparison with PINOT with both simulated and real MRI data. To evaluate temporal fidelity, temporal plots of signal intensity along two lines were shown as well. TSENSE and *k-t* SENSE mean signal intensities are compared with PINOT along the spatial and temporal dimensions, noise distribution histogram of three methods are shown as well. Computational cost of different methods is also analyzed.

In the fourth experiment, we compared noise level of the PINOT reconstructions using the default subset sampling schemes with the TSENSE, *k-t* SENSE sampling schemes (Fig. 1d,e). Additionally, two criteria, condition number and sum of squared errors, were shown to demonstrate the numerical stability of PINOT encoding matrix associate with different sampling schemes. Assuming added gaussian distributed noise and the least squared reconstruction, sum of squared errors (SSE) (25,26) of the PINOT reconstructed image is measured using $E_{(M_{PINOT})} = \text{trace}\{(M_{PINOT}^H \psi M_{PINOT})^{-1}\}$. Here Ψ is the receiver noise covariance matrix and considered as identity matrix for simplicity.

In experiment five, regularized PINOT was implemented using Tikhonov regularization (27). Low-resolution reference (25% of full-resolution phase encoding lines) scan is used as a prior estimate of the solution. The regularization parameter was calculated using L-curve algorithm (28). We compared PINOT with/without regularization under two different reduction factors 3.75 and 13.33 (75% static FOV for Noquist and $R_{np} = 4$). All experiments were computered in MATLAB R2007a (The Mathworks, Natick, MA) on a QuadCore Xeon 2.66 GHz workstation with 16 GB of RAM.

Data

Computer simulation data: A time-resolved 2D computer generated data set [see (14)] was generated to simulate MRI acquisition of cardiac motion, with 120 frequency and phase encoding samples and 15 temporal frames. Four surface coils were simulated, located at each side of the FOV. The magnitude of the coil's sensitivity maps was calculated by the Biot-Savart law (29). Geometric phase warp patterns (differently angled linear warps) were applied to each complex sensitivity map to avoid

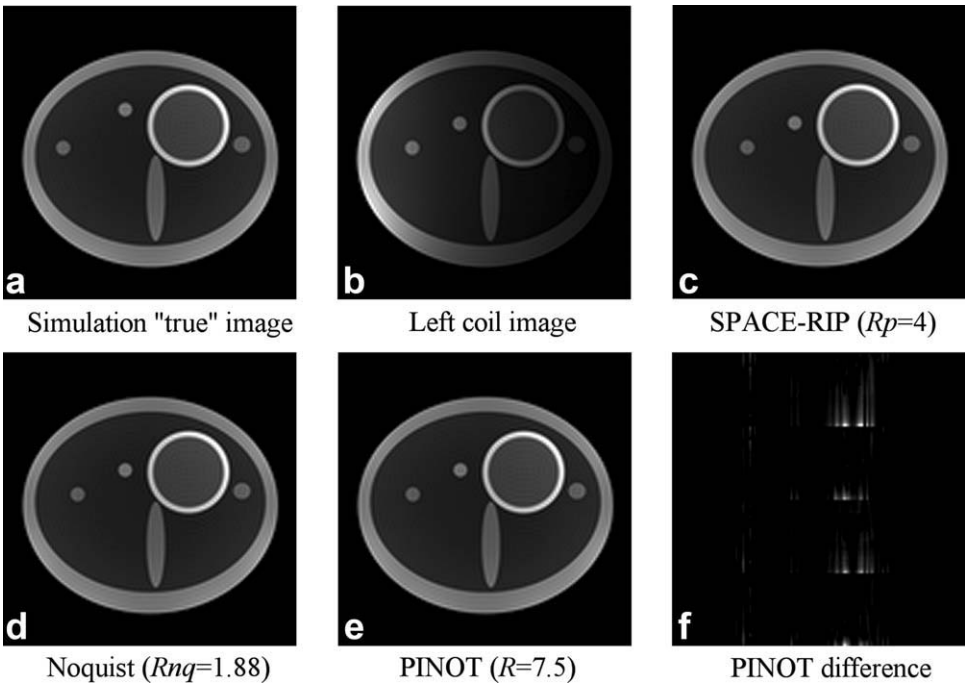

FIG. 2. The figures show the 1st frame of 15 from a computer simulated sequence for: (**a**) full-grid reconstructed "true" image, (**b**) left surface coil computer simulated image, (**c**) SPACE-RIP reconstruction with reduction factor 4, (**d**) Noquist reconstruction with 50% centrally located dynamic FOV (reduction factor $R = 1.88$), (**e**) PINOT reconstruction (reduction factor $R = 7.5$), and (**f**) is the amplified absolute difference between PINOT and full-grid reconstruction, scaled up by a factor of 1000. Differences between truth and Noquist and SPACE-RIP reconstructions were smaller yet than for PINOT.

unrealistic phase symmetry and the associated impact on the condition of the inversion problem, as previously described by Kyriakos (7).

MRI data: Breath-held, prospectively gated steady-state free precession cardiac MRI scans were used to evaluate PINOT by a protocol approved by the Institutional Review Board. The full Cartesian *k*-space data were used as ''truth'' images for comparison. Data sets are from a GE 1.5 T TwinSpeed scanner (R12M4) using an 8-element cardiac coil. For a 2-chamber view cine MRI scan, a FIESTA/FastCARD cine steady-state free precession sequence was used with slice thickness 8 mm, TR = 4.4 msec, TE = 1.5 msec, flip angle 45°, 192 phase encodings, 224 read-out samples, and 12 temporal frames. Sensitivity maps were estimated from the same data to simulate perfectly co-registered maps. We note that this approach introduces a positive bias in the observed SNR, but eliminates complications from misregistration, which may otherwise be confused with residual artifact due to the method itself. A short axis MRI scan was acquired using a FIESTA/FastCARD cine steady-state free precession sequence. Scan parameters: TE = 2.0 msec, TR = 4.1 msec, flip angle = 45°, FOV = 350 × 350 mm, slice thickness = 12 mm, 8 views per segment, 202 phase encoding views (zero-padded to 224), 256 read-out samples, and 16 temporal frames. For this acquisition, a separate reference scan was obtained within the same breathhold with identical scan parameters to estimate sensitivity maps. Sensitivity maps were calculated from reference scan data. Both sensitivity maps were estimated as follows: first the (50%) highest frequency *k*-space views for each coil were removed. An inverse Fourier transform was applied to obtain the smoothed coil image after applying a smoothing filter. These images were subsequently divided by the root-sum-of squares of all coil images to estimate the sensitivity maps.

Comparison of PINOT, k-t SENSE and TSENSE

To compare PINOT with TSENSE (16) and *k-t* SENSE (19), reconstruction problems were dimensioned to achieve approximately the same acceleration factors for all three methods. To ensure a fair comparison, the same sensitivity map was used for all three methods. Modified TSENSE (16) was implemented combining UNFOLD ($R = 2$) with SENSE ($R = 2$). With the simulation data, 10 additional training data profiles were acquired for *k-t* SENSE with reduction factor 4. For PINOT, a SENSE reduction factor of 2 was used, and a 50% dynamic FOV for Noquist. These parameters yield reduction factors of 4 for TSENSE, *k-t* SENSE, and 3.75 for PINOT with simulated data. In a short axis MRI scan, the same settings were applied with corresponding reduction factors 4 for TSENSE, *k-t* SENSE, and 3.73 for PINOT. Extensions of the sampling patterns of Fig. 1 were used for all reconstructions.

Quantitative Performance Evaluation

As in Refs. 23 and 24, we define SNR of each pixel in the reconstructed image as the ratio of the pixel's mean value to its standard deviation across several acquisitions differing only in noise. In our experiments, gaussian noise was added to the real and imaginary parts of the simulated data, with noise level comparable with that measured in real MR images. The reconstruction process was repeated 200 times for different realization of the random noise. The mean signal intensity is calculated by taking the average of the all reconstructed magnitude images for each pixel. The noise level is then calculated by taking the standard deviation in the resulting image magnitudes for each pixel, divided by the square root of reduction factor to normalize for different acceleration factors.

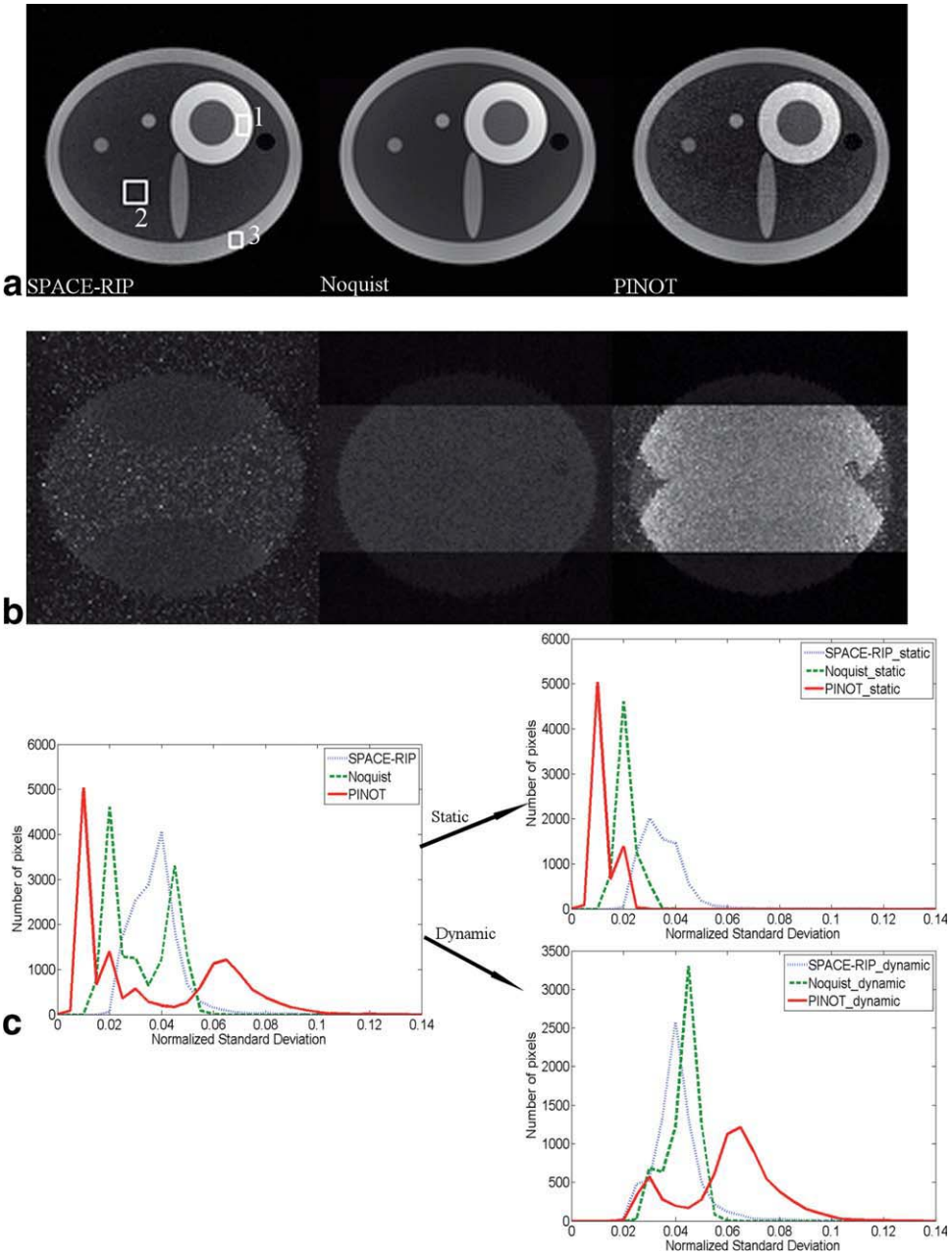

FIG. 3. Reconstructed images (frame 7) of SPACE-RIP, Noquist, and PINOT showing (**a**) the mean signal intensities, (**b**) the normalized noise standard deviations, and (**c**) the corresponding histogram within full reconstructed images, compared with only the static and dynamic reconstructed regions images. [Color figure can be viewed in the online issue, which is available at wileyonlinelibrary.com.]

RESULTS

Computer Simulated Data Reconstruction

Figure 2 shows experimental results comparing SPACE-RIP, Noquist and PINOT for noiseless computer simulated data. We used reduction factors of $R_p = 4$ for SPACE-RIP (Fig. 2c) and $R_{nq} = 1.88$ for Noquist (Fig. 2d) with 15 frames and 50% dynamic FOV. PINOT reconstruction (Fig. 2e) achieved a reduction factor of $R = 7.5$, or using only about 14% of phase encoding samples. Figure 2f shows the difference image (absolute intensity differences with the full-grid ''true'' image), scaled up by a factor of 1000. These experiments demonstrate PINOT reconstruction under ideal noiseless conditions.

With added gaussian noise, the mean signal of magnitude and the noise distribution of SPACE-RIP ($R = 2$), Noquist ($R = 1.88$) and PINOT ($R = 3.75$) are presented in Fig. 3. As in Noquist (14), PINOT noise distribution shows higher noise levels in the dynamic FOV. As in parallel imaging (6), we observe higher noise levels at locations with low coil sensitivity than at locations with high sensitivity. Both Noquist and PINOT showed a similar two peak shape with wider range noise distributions compared with SPACE-RIP. This occurs because the Noquist and PINOT reconstruction results in different noise level in static and dynamic region. The explanation is confirmed by the histograms displaying the static region and dynamic region normalized noise distribution separately.

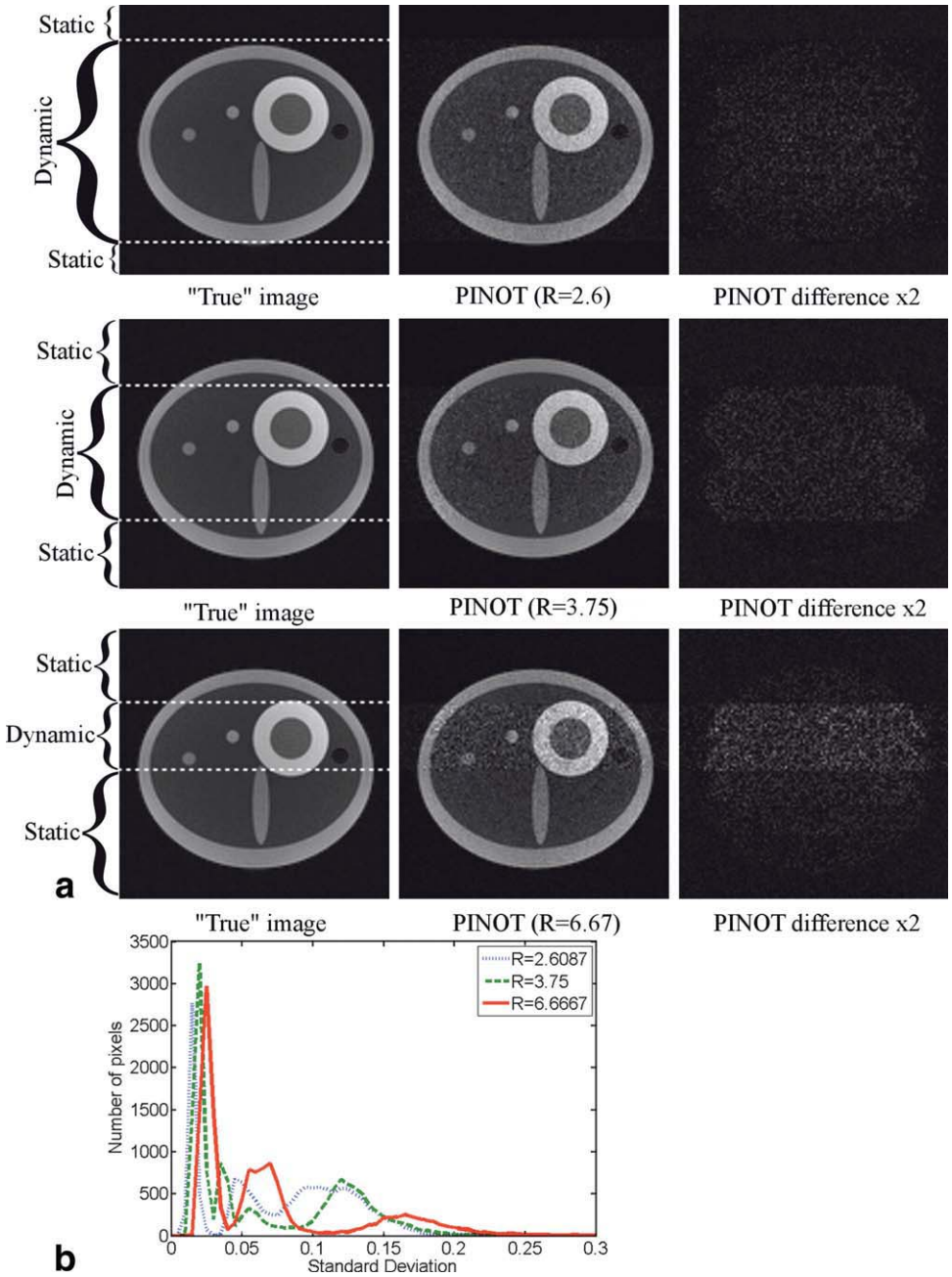

FIG. 4. **a**: PINOT reconstructions of 7th frame from the computer simulated images with noise. Each row includes: "True" image reconstructed using full samples, PINOT reconstruction with different reduction factor, and difference image. All reconstructions are shown at the same intensity scale. Intensities in the difference image are amplified by a factor of 2 to see the details. Static and dynamic regions for PINOT are marked in "True" images. **b**: Histogram curves of the noise standard distribution for PINOT with reduction factors 2.6, 3.75, and 6.67. [Color figure can be viewed in the online issue, which is available at wileyonlinelibrary.com.]

PINOT reconstructions were tested with three different reduction factors (R = 2.61, 3.75, 6.67), corresponding R_p = 2 and 25%, 50%, and 75% static FOV for Noquist (Fig. 4). Even with noisy data and sensitivity maps, PINOT is still able to capture image changes at sharp edges and preserves spatiotemporal resolution well, but at a cost of reduced SNR, especially in the dynamic region. Figure 4b showed the noise level histograms for PINOT with different acceleration factors. Table 1 shows the means, ranges of condition numbers observed in M_{PINOT}, and reconstructed errors associated with different acceleration factors (R = 3.75, 6.67, 13.33). Clearly, the higher is the reduction factor, the less is well-condition M_{PINOT}, the noisier is PINOT reconstruction.

Cine MRI Scans

SPACE-RIP, Noquist, and PINOT reconstructions, cropped to the heart region, of a two-chamber view cardiac MRI scan are shown in Fig. 5. The conventional, SPACE-RIP, Noquist, and PINOT reconstructions used 192, 96, 104, and 52 phase encodings per frame, respectively, corresponding with reduction factors of 1, 2, 1.85, and 3.7.

Figure 6 shows PINOT reconstructions (frames 1, 9, and 15) of a 16-frame short axis scan. The PINOT reduction factor is 3.76, combining SPACE-RIP reduction

Table 1
Condition Number Range, Mean and Reconstruction Error for PINOT With Reduction Factors (R = 3.75, 6.67, 13.33)

R_{PINOT}	$R_{SPACE\text{-}RIP}$	$R_{Noquist}$	Condition number range	Condition number mean	Reconstruction error (frame 1)
3.75	2	1.875	[7.214 26.589]	12.472	11.216
6.67	2	3.33	[12.340 31.119]	21.819	14.3897
13.33	4	3.33	[132.17 1334.65]	590.382	93.4515

factor 2 and Noquist reduction factor 1.88 (50% dynamic FOV). These PINOT reconstruction results both further confirm the edge detail preservation and reduced SNR, observed in the reconstructions from computer simulated data.

Comparison of PINOT With *k-t* SENSE and TSENSE

Figure 7a compares, in spatial domain, TSENSE, *k-t* SENSE, and PINOT at simulated diastole and systole for noisy computer simulated data. All three methods yielded visually acceptable image quality for acceleration factors at or close to 4. TSENSE and *k-t* SENSE both displayed residual edge blurring at myocardial boundaries and image artifacts (marked by white arrows) during systolic contraction and diastolic relaxation. PINOT showed noticeably less edge artifact; however, at some penalty of higher random noise level, especially in the dynamic FOV region. Mean signal intensity images and the normalized noise distribution histogram (Fig. 7c) further confirm this observation. A corresponding comparison in a short axis MRI scan is shown in Fig. 8, cropped to a region around the heart to highlight important myocardial edge details. The comparison of PINOT, TSENSE, and *k-t* SENSE consistently shows the same observation regarding edge resolution and SNR. These findings for TSENSE and *k-t* SENSE agree with prior reports (30–32).

For the comparison of intensity changes over time, temporal profiles of two 1D spatial cuts along the phase encoding axis are presented for the noisy computer simulated and short axis images, at two readout locations each, in Figs. 7b and 8d. Mean signal intensity images and the normalized noise distribution histogram are shown in Fig. 7c. The time

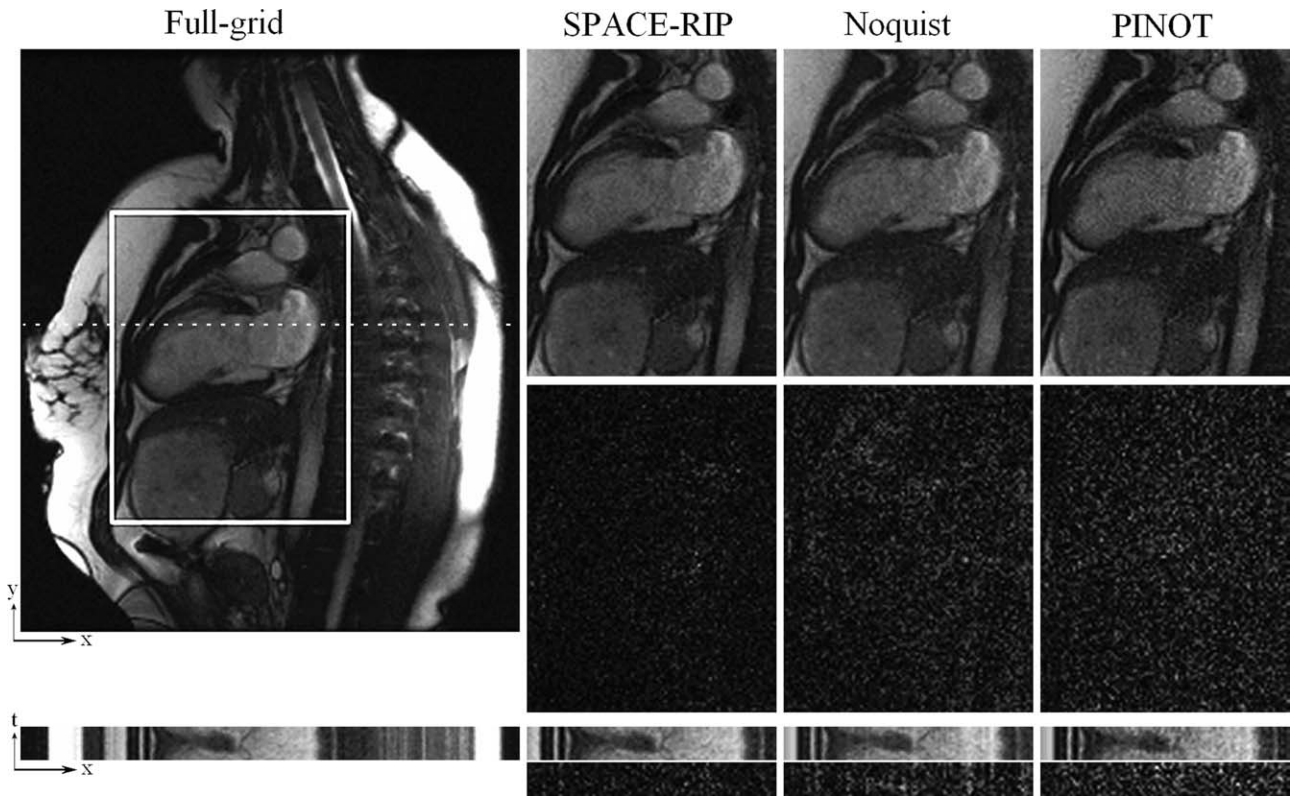

FIG. 5. Comparison of a conventional full grid acquisition, SPACE-RIP reconstruction with a reduction factor of 2, Noquist reconstruction with 50% dynamic FOV (reduction factor is 1.85), and PINOT reconstruction with a reduction factor of 3.7 for real MRI data with a two-chamber long-axis view of the heart region (frame 1 of 12). Differences are shown at bottom with corresponding reconstructed ROI images. Temporal direction and difference are shown below full-grid image and each reconstructed image. The differences are scaled up by a factor of 5 to reveal details.

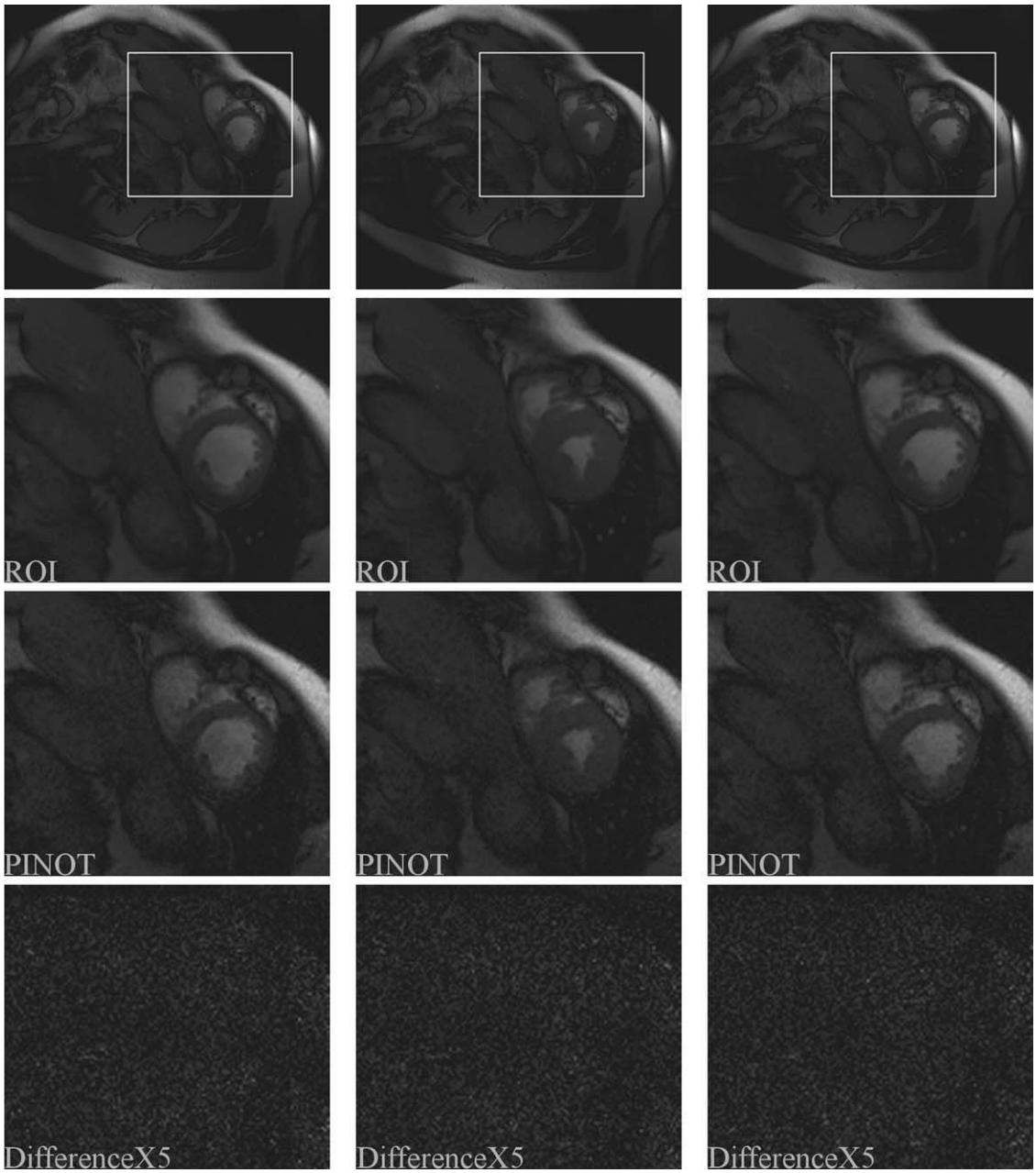

FIG. 6. Conventional full-grid "true" images results (top row) and enlarged ROI (2nd row) for a retrospectively sub-sampled real MRI scan, compared with PINOT ($R = 3.76$) (3rd row) for three different image frames (frames 1, 9, and 15 of a 16 frame series). The bottom row shows the corresponding difference images (with an intensity multiplication factor of 5).

profiles from the (cropped) short axis scan (Fig. 8d) were selected through the septal wall and the left ventricle (LV) myocardium. In both cases, these results again confirm that PINOT better captures the changes over time at sharp edges, as evidenced by the bright vertical lines (arrows) in the difference images for *k-t* SENSE and TSENSE at end systole, which indicate edge errors. PINOT shows a higher uniform noise level across the (x-t) difference map, whereas TSENSE and *k-t* SENSE results show remarkable gap of sharp signal transition along temporal frames (marked in white arrows). In Fig. 8, TSENSE shows a signal loss at the right ventricle wall, and TSENSE and *k-t* SENSE both have signal loss near abrupt systolic intensity changes near the endocardial edge. When comparing with TSENSE and *k-t* SENSE in temporal direction, PINOT has a slightly higher noise level in the dynamic FOV (Fig. 8c) but lower noise level in the static FOV.

The PINOT reconstruction computational time was measured for the phantom data set ($M_{\mathrm{PINOT}} = 1920 \times 960$, $R = 3.75$). Direct matrix inversion for all 120 readout pixels by MATLAB on a Quad Core Xeon 2.66 GHz computer with 16 GB of RAM requires 58 min. However, this computational cost can be alleviated by using iterative conjugate gradient method down to 6.38 min. For comparison: TSENSE reconstruction ($R = 4$) and *k-t*

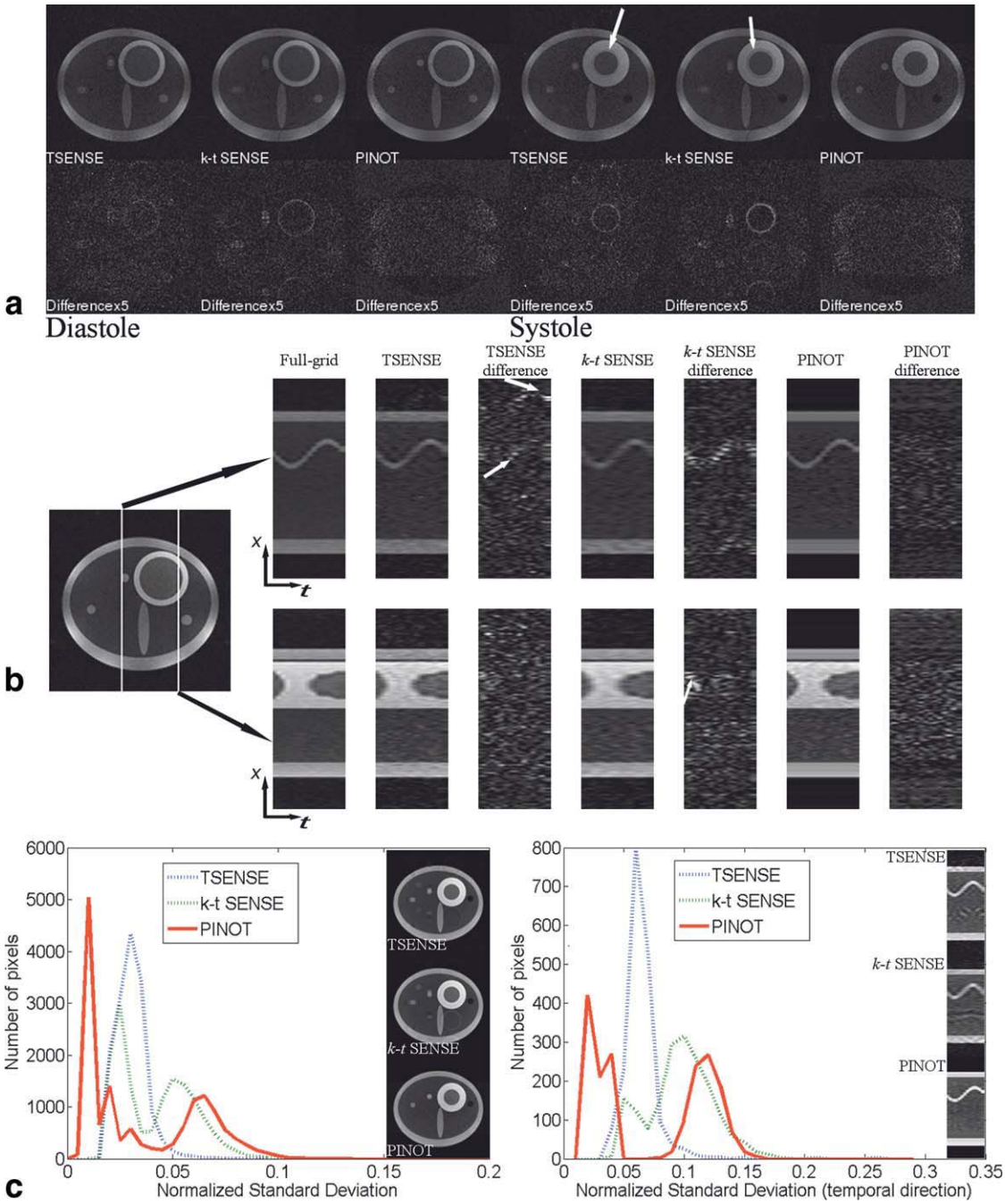

FIG. 7. TSENSE, *k-t* SENSE, and PINOT reconstruction comparison of the diastole and systole frames from a 15-frame computer simulated data set with noise. Row **a**: TSENSE reconstruction (reduction factor = 4), *k-t* SENSE reconstruction (reduction factor = 4) and PINOT reconstruction with 50% dynamic FOV (reduction factor = 3.75). The absolute differences between TSENSE, *k-t* SENSE, and PINOT with the full-grid reconstruction are also displayed (difference images are enlarged 5 times to see the details, then all the images are shown under the same scale). **b**: The corresponding profiles in *y-t* space at different *x*. Gap of sharp signal transition and image artifacts along temporal frames are marked in white arrow. **c**: The histograms of the noise level with mean signal intensity images along spatial and temporal direction (All images are under the same scale). [Color figure can be viewed in the online issue, which is available at wileyonlinelibrary.com.]

SENSE ($R = 4$) of the same data set required and 0.65 and 0.95 min, respectively.

PINOT Sampling Scheme Comparisons

Figure 9 shows the histogram of noise level, using all three different sampling schemes on PINOT around reduction factor 4. We found that the sampling pattern we proposed is slightly better than the other two. Table 2 shows the condition numbers from two columns shown in Fig. 7b and sum of squared errors of M_{PINOT} with three different sampling schemes. All three sampling schemes generate comparable well conditioned PINOT encoding matrix and PINOT sampling scheme has the smallest sum of squared errors.

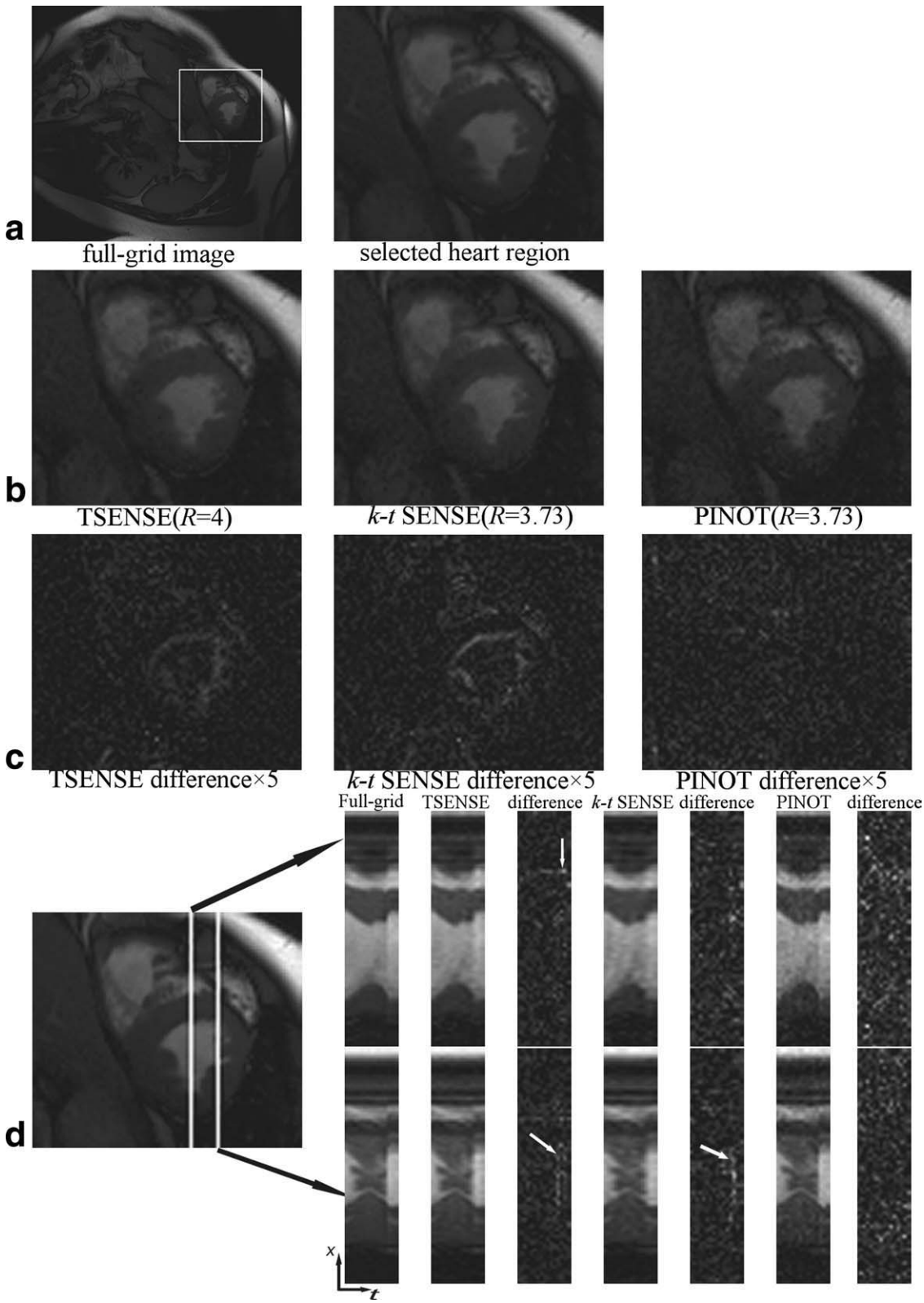

FIG. 8. 13th of 16 frames in an axial data set, comparing the selected heart region from the full-grid image and the reconstructed image from TSENSE, *k-t* SENSE, and PINOT. **a**: Full-FOV image and zoomed ROI images to reveal details in the heart. Zoomed TSENSE, *k-t* SENSE and PINOT results are shown in (**b**). **c**: The corresponding difference images between selected heart region from the full-grid image and TSENSE, *k-t* SENSE, and PINOT, all amplified by the same factor 5 to compare differences. The achieved reduction factor is 4 for TSENSE, *k-t* SENSE, and 3.73 for PINOT. Corresponding profiles in *y-t* space at different *x* were shown at the (**d**). Gap of sharp signal transition along temporal frames are marked in white arrow (All images are under the same scale).

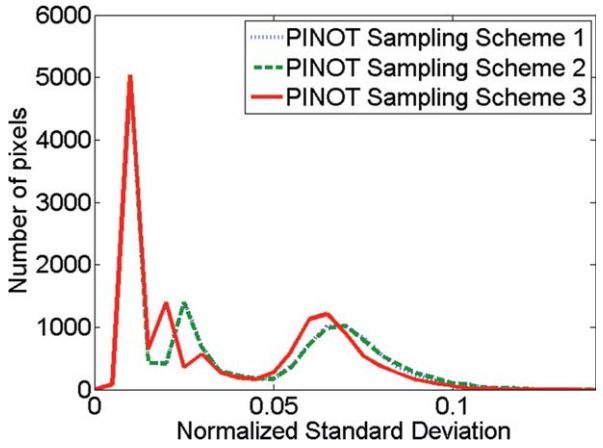

FIG. 9. Normalized noise distribution for PINOT with three different sampling patterns. PINOT sampling scheme from 1 to 3 is TSENSE, *k-t* SENSE, and PINOT sampling scheme, respectively. [Color figure can be viewed in the online issue, which is available at wileyonlinelibrary.com.]

PINOT Regularization

As what we observe from Fig. 10a, there is no noticeable difference with/without regularization for PINOT reconstruction with $R = 3.75$. When the reduction factor is high ($R = 13.33$), noise amplification penalty of unregularized PINOT becomes a dominating factor in image quality, shown in Fig. 10b, while regularized PINOT reconstruction shows a significant SNR improvement, but loses edge information. The observation is consistent with the assertion in (27) that the use of lower spatial resolution reference images as the regularization prior may result in oversmoothed reconstructed images. We conclude that PINOT with regularization may sacrifice edge detail in exchange of SNR improvement.

DISCUSSION

Overall, PINOT has yielded stable results with a composite acceleration rate of around 3.5–4 for both simulated data and a variety of MRI data sets. In all experiments where the constituent Noquist and SPACE-RIP methods yielded high-quality results, we also observed satisfactory image quality with the corresponding PINOT reconstruction. PINOT effectively achieves multiplication of the individual acceleration factors of the constituent methods, and intuitively that it should come with a corresponding accumulated cost in SNR penalties in the dynamic region. A 50% static FOV for Noquist and a reduction factor of 2 for parallel imaging appear to be reasonable parameters for cine cardiac images with 4–8 channel flexible surface coils at 1.5 T, resulting in a composite acceleration rate of around 4. In such cases PINOT encoding matrix is well conditioned and the PINOT reconstruction can be solved by iterative conjugate gradient method to alleviate the high-computational cost of the direct matrix inversion. For the cases when images have implicitly low SNR, or high-acceleration factor, the noise amplification penalty of PINOT may become a dominating factor in image quality. Regularization must be applied to improve the SNR, but may lose edge details and have increased computational burden.

When compared with TSENSE and *k-t* SENSE at similar sampling rates, PINOT has better edge preservation and higher temporal resolution, but with higher random noise level in dynamic regions. An explanation for these may be the fact that as a combination of Noquist and SPACE-RIP, PINOT does not apply any filter or implicit regularization. In clinical analysis of cardiac function, accurate detection of myocardial boundary locations is critically important. From this perspective, PINOT has a spatial-temporal resolution advantage, but this must be weighed against the SNR penalty.

In most reconstructions in this study, we simply extended the Noquist sampling pattern with the straightforward even-spaced subsampling commonly used parallel imaging. Our experiments also showed the possibilities of using TSENSE or *k-t* SENSE sampling patterns, but with slightly higher noise level results.

PINOT reconstruction involves a large matrix inversion for each read-out coordinate through combining all time frames and coils. A solution for alleviating the high-computational cost of direct matrix inversion is the use of iterative conjugate gradient algorithms. However, because the matrix is relatively sparse, an alternative using special sparse-matrix data structures to further increase the reconstruction speed are currently under investigation. Additional savings in computation time may be realized by more extensive use of parallel computing, for example using recently popularized GPU processing methods (33,34).

CONCLUSIONS

The PINOT method integrates SPACE-RIP parallel imaging with Noquist rFOV to accelerate cine imaging with acceleration factor that equal the product of the

Table 2
Condition Number and Sum of Squared Errors (Two Columns) for PINOT Reconstruction With Three Different Sampling Schemes

PINOT Sampling Scheme	Condition number Column 49	SSE Column 49	Condition number Column 87	SSE Column 87
1 (TSENSE Sampling)	8.1122	35.6672	11.7889	40.6622
2 (*k-t* SENSE Sampling)	8.0523	35.6749	11.3010	40.6202
3 (PINOT Sampling)	8.3487	33.9941	14.8061	39.7927

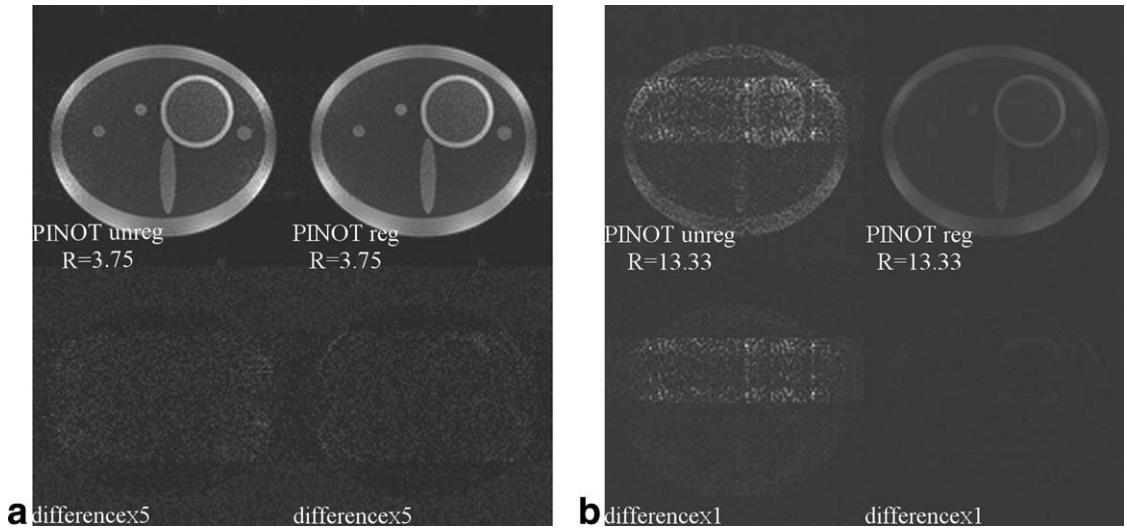

FIG. 10. Unregularized and regularized computer simulated PINOT reconstruction of (**a**) reduction factor 3.75 and (**b**) reduction factor 13.33 using reference scan at 25% spatial resolution. Corresponding difference images are shown below, scaled by 5 in (a) to show details.

individual factors feasible for each method. As illustrated by computer simulated and real MRI data experiments, PINOT can be successfully applied to the reconstruction of undersampled MR images while preserving full spatial-temporal resolution, retaining edge information better than comparable methods like TSENSE and *k-t* SENSE around reduction factor 4. However, the PINOT algorithm adds to the computational burden of the image reconstruction, and cost in accumulated SNR penalty in dynamic regions. If an SNR trade-off can be afforded, PINOT may be the method of choice for accelerated acquisition with full preservation of sharp edge details. For imaging systems with limited SNR, TSENSE and *k-t* SENSE may be more suitable methods. Continued research must focus on reducing the computational cost associated with this acceleration technique.

ACKNOWLEDGMENTS

The authors thank Dr. Sebastian Kozerke for the help with implementation of *k-t* BLAST and *k-t* SENSE and Dr. Robert Butera of Georgia Tech for tireless and selfless help in administrative matters. They also thank reviewers for all the useful comments.

REFERENCES

1. Sodickson DK, Manning WJ. Simultaneous acquisition of spatial harmonics (SMASH): fast imaging with radiofrequency coil arrays. Magn Reson Med 1997;38:591–603.
2. Jakob PM, Griswold MA, Edelman RR, Sodickson DK. AUTO-SMASH: a self-calibrating technique for SMASH imaging, SiMultaneous Acquisition of Spatial Harmonics. MAGMA 1998;7:42–54.
3. Heidemann RM, Griswold MA, Haase A, Jakob PM. VD-AUTO-SMASH imaging. Magn Reson Med 2001;45:1066–1074.
4. Griswold M, Jakob P, Heidemann R, Nittka M, Jellus V, Wang J, Kiefer B, Haase A. Generalized autocalibrating partially parallel acquisitions (GRAPPA). Magn Reson Med 2002;47:1202–1210.
5. Griswold M, Jakob P, Nittka M, Goldfarb J, Haase A. Partially parallel imaging with localized sensitivities (PILS). Magn Reson Med 2000; 44:602–609.
6. Pruessmann KP, Weiger M, Scheidegger MB, Boesiger P. SENSE: sensitivity encoding for fast MRI. Magn Reson Med 1999;42:952–962.
7. Kyriakos WE, Panych LP, Kacher DF, Westin CF, Bao SM, Mulkern RV, Jolesz FA. Sensitivity profiles from an array of coils for encoding and reconstruction in parallel (SPACE RIP). Magn Reson Med 2000; 44:301–308.
8. Ohliger MA, Grant AK, Sodickson DK. Ultimate intrinsic signal-to-noise ratio for parallel MRI: electromagnetic field considerations. Magn Reson Med 2003;50:1018–1030.
9. Wiesinger F, Boesiger P, Pruessmann KP. Electrodynamics and ultimate SNR in parallel MR imaging. Magn Reson Med 2004;52:376–390.
10. Ying L, Sheng J. Joint image reconstruction and sensitivity estimation in SENSE (JSENSE). Magn Reson Med 2007;57:1196–1202.
11. Uecker M, Hohage T, Block KT, Frahm J. Image reconstruction by regularized nonlinear inversion—joint estimation of coil sensitivities and image content. Magn Reson Med 2008;60:674–682.
12. Hoge WS, Brooks DH. Using GRAPPA to improve autocalibrated coil sensitivity estimation for the SENSE family of parallel imaging reconstruction algorithms. Magn Reson Med 2008;60:462–467.
13. Madore B, Glover GH, Pelc NJ. Unaliasing by fourier-encoding the overlaps using the temporal dimension (UNFOLD), applied to cardiac imaging and fMRI. Magn Reson Med 1999;42:813–828.
14. Brummer ME, Moratal-Perez D, Hong C, Pettigrew R, Millet-Roig J, Dixon W. Noquist: reduced field-of-view imaging by direct Fourier inversion. Magn Reson Med 2004;51:331–342.
15. Kellman P, Epstein FH, McVeigh ER. Adaptive sensitivity encoding incorporating temporal filtering (TSENSE). Magn Reson Med 2001; 45:846–852.
16. Kellman P, Epstein FH, McVeigh ER. The development of TSENSE. In: Schoenberg SO, Reider MF, editors. Parallel imaging in clinical MR applications. Heidelberg: Springer; 2007.
17. Madore B. UNFOLD-SENSE: a parallel MRI method with self-calibration and artifact suppression. Magn Reson Med 2004;52:310–320.
18. Breuer FA, Kellman P, Griswold MA, Jakob PM. Dynamic autocalibrated parallel imaging using temporal GRAPPA (TGRAPPA). Magn Reson Med 2005;53:981–985.
19. Tsao J, Boesiger P, Pruessmann KP. k-t BLAST and k-t SENSE: dynamic MRI with high frame rate exploiting spatiotemporal correlations. Magn Reson Med 2003;50:1031–1042.
20. Barrett HH, Myers KJ. Foundations of image science. Saleh B, editor. Hoboken, NJ: Wiley; 2003.
21. Pruessmann KP, Weiger M, Bornert P, Boesiger P. Advances in sensitivity encoding with arbitrary k-space trajectories. Magn Reson Med 2001;46:638–651.
22. Moratal D, Brummer M, Dixon W. Optimal data sampling for Noquist ciné imaging. In: Proceedings of the 14th Annual Meeting of ISMRM, May 6–12, Seattle, WA, USA, 2006.

23. Thunberg P, Zetterberg P. Noise distribution in SENSE- and GRAPPA-reconstructed images: a computer simulation study. Magn Reson Imaging 2007;25:1089–1094.
24. Dietrich O, Raya JG, Reeder SB, Reiser MF, Schoenberg SO. Measurement of signal-to-noise ratios in MR images: influence of multichannel coils, parallel imaging, and reconstruction filters. J Magn Reson Imaging 2007;26:375–385.
25. Jacob M, Xu D, Liang Z-P. Optimal selection of phase encoding in parallel MR imaging, Proc. Second International Workshop on Parallel MRI, Zurich, 2004.
26. Reeves SJ, Zhe Z. Sequential algorithms for observation selection. IEEE Trans Signal Process 1999;47:123–132.
27. Lin FH, Kwong KK, Belliveau JW, Wald LL. Parallel imaging reconstruction using automatic regularization. Magn Reson Med 2004;51: 559–567.
28. Hansen PC. Regularization tools: a Matlab package from analysis and solution of discrete ill-posed problems. Numer Algorithms 1994;6: 1–35.
29. Cheng DK. Field and wave electromagnetics. Reading, Mass.: Addison-Wesley; 1989.
30. Pedersen H, Kozerke S, Ringgaard S, Nehrke K, Kim WY. k-t PCA: temporally constrained k-t BLAST reconstruction using principal component analysis. Magn Reson Med 2009;62:706–716.
31. Gamper U, Boesiger P, Kozerke S. Compressed sensing in dynamic MRI. Magn Reson Med 2008;59:365–373.
32. Xu D, King KF, Liang ZP. Improving k-t SENSE by adaptive regularization. Magn Reson Med 2007;57:918–930.
33. Sorensen T, Atkinson D, Boubertakh R, Schaeffter T, Hansen M. Rapid non-cartesian parallel imaging reconstruction on commodity graphics hardware. In: Proceedings of the 16th Annual Meeting of ISMRM, Toronto, ONT, 2008. p 1490.
34. Haldar J, Stone S, Yi H, Tsao SC, Sutton BP, Hwu W-MW, Liang ZP. Fast MR image reconstruction using graphics processing units. In: Proceedings of the 16th Annual Meeting of ISMRM, Toronto, Canada, 2008. p 1493.